De novo design of metalloproteases for targeted amyloid-β cleavage

Yannan Qu [1, 2, †], Chentong Wang [1, 2, †], Hongli Zhu[1,2], Yanjun Wang[1,2], Longxing Cao[1,2*]

1. State Key Laboratory of Gene Expression, School of Life Sciences, Westlake University, Hangzhou 310024, China.

2. Artificial Intelligence Drug Design Core Laboratory, Westlake Laboratory of Life Sciences and Biomedicine, Hangzhou, Zhejiang, 310024, China.

*Corresponding author. E-mail: caolongxing@westlake.edu.cn

† These authors are co-first authors.

Abstract

De novo protein design has not yet achieved the creation of proteases capable of selectively cleaving any desired peptide bond within a native protein with high precision. Here, we report the use of the flow-based generative model Proteus2 to design metalloproteases by generating enzyme–substrate complexes conditioned on a target peptide sequence and a predefined catalytic motif. Our approach employs a two-step encapsulation strategy to create clamp-like metalloproteases that bind the target peptide in a manner that maximizes substrate sequence specificity. The generative process simultaneously optimizes the precise positioning of the target peptide bond in a catalytically competent configuration and accurately scaffolds the transition state catalytic residues—both essential for specific and efficient catalysis. Using this strategy, we designed zinc metalloproteases targeting three distinct cleavage sites within the aggregation-prone regions of amyloid-β (Aβ), a key pathogenic factor in Alzheimer's disease. Experimental characterization validated five enzymes, each capable of precise cleavage at the intended sites with high specificity and minimal or undetectable activity on non-cognate substrates. On average, these enzymes accelerated peptide bond hydrolysis by more than 10^7-fold relative to the uncatalyzed reaction , and enabled efficient digestion of the Aβ peptide into smaller segments when enzymes targeting different sites were combined. Cryo-EM structures of three designed enzymes in complex with Aβ peptide, each targeting a distinct cleavage site, revealed close agreement with the design models. Together, these results demonstrate the potential of sequence-guided, generative approaches for developing programmable, sequence-specific proteolysis and lay the groundwork for future applications in basic research and therapeutic development.

Introduction

Proteases are among biology's most powerful regulators[1,2]. By cutting specific peptide bonds they activate hormones[3], terminate signalling cascades[4], remodel extracellular matrices[5], and control protein homostasis[1]. Their catalytic activity also underpins a wide spectrum of industrial and medical applications—from laundry detergents and food processing to wound debridement and thrombolytic therapy[6,7]. Yet the utility of natural proteases is circumscribed by their hard-wired substrate preferences[8,9]. An enduring objective is therefore to create "molecular scalpels" whose cleavage site can be programmed at will, enabling precise dissection of cellular pathways and highly selective therapeutic intervention[10,11]. Despite decades of effort, very few platform delivers custom proteases that combine robust catalytic efficiency with single-bond specificity[12-14].

Metalloproteases are prime candidates for such re-engineering, and their catalytic chemistry has been well studied[15-17]. In a typical zinc metalloprotease, the zinc ion is coordinated by three amino-acid ligands and positioned adjacent to a general base that activates a water molecule for nucleophilic attack on the peptide bond, while a neighbouring residue stabilises the tetrahedral oxyanion intermediate[17] (**Fig. 1a,b**). This minimalist engine is embedded in diverse scaffolds—including matrix metalloproteinases[18], ADAMs[19], astacins[20], thermolysins[21], and bacterial virulence factors[22]—that collectively drive processes from extracellular-matrix turnover to cytokine maturation. Despite their natural versatility, repurposing these enzymes for novel targets remains challenging. While efforts to reprogram specificity through directed evolution or rational mutagenesis have yielded promising advances[12,13,23], certain structural and functional limitations persist. As a result, repurposed natural metalloproteases have achieved only modest improvements in selectivity and therapeutic potential[24].

De novo protein design holds the promise of sidestepping the intrinsic limitations of natural enzymes by constructing entirely new scaffolds around a chosen chemical task[25-29]. Recent breakthroughs in deep-learning based structure generation have indeed delivered artificial metallohydrolases whose catalytic efficiencies approach those of native enzymes[26,28,30]; however, these successes have been confined almost exclusively to model reactions such as the hydrolysis of activated ester bonds in small, hydrophobic substrates—reactions that present relatively low activation barriers and low specificity demands. Extending this progress to true proteolysis is vastly more challenging. Amide bonds are orders of magnitude more inert than esters[31,32], and a protease must not only accelerate their cleavage but also capture a highly flexible, polar peptide and orient one particular bond in a near-attack conformation. Moreover, practical applications require a high level of sequence selectivity, such that the designed substrate binding groove preferentially accommodates the target sequence while minimizing activity toward closely related peptides. Natural proteases achieve this balance with folds that have been evolutionarily honed for cognate substrates; even slight structural perturbations can disrupt the sub-angstrom precision of the catalytic residues[9,33]. Consequently, conventional sequence redesign has limited success in retargets these enzymes while maintaining native-like catalytic efficiency[33-36]. The central challenge, therefore, is to design new structures that simultaneously preserve the strict metal-dependent catalytic geometry, lock the scissile bond into position, and rigorously discriminate against off-target sequences—an objective that has so far remained out of reach.

Computational strategy for designing sequence specific metalloprotease

We set out to develop a general strategy for the de novo design of sequence-specific metalloproteases. To establish catalytic motifs for design, we focused on two representative zinc-

dependent endopeptidases: PPEP-1 (PDB: 6r4w) [37] and Fungalysin (PDB: 4k90) [38]. Both enzymes are secreted by microorganisms and play critical roles in survival or pathogenicity by hydrolyzing extracellular host or cell-surface proteins. Despite sharing a common catalytic mechanism, these two enzymes exhibit distinct active site architectures. Notably, their oxyanion hole compositions differ: PPEP-1 employs a tyrosine, whereas Fungalysin utilizes a histidine residue. Structurally, PPEP-1 features a broad, clamp-like groove formed by two flexible loops that close over the substrate, conferring high sequence specificity for cleavage at Pro-Pro amide bonds. To reprogram this specificity, we developed a strategy that removes the peptide-binding loops from PPEP-1, while retaining the core protein structure (**Fig. 1c**). The excised regions were then rebuilt, enabling the design of new peptide-binding interfaces. Proteases designed through this approach are denoted "PP" (peptide-binding pocket designed protease) followed by a numerical identifier. In contrast, Fungalysin lacks an extended, pre-formed substrate-binding pocket and instead features an open substrate binding groove, resulting in a broader substrate specificity for peptide bonds flanked by hydrophobic side chains. For this scaffold, we extracted only the minimalist catalytic motif—comprising the zinc-coordinating residues, the general base glutamate, and the oxyanion hole histidine (**Fig. 1c**). This minimalist approach necessitates de novo generation of the entire surrounding protein scaffold to accurately position the catalytic motif and design a novel peptide-binding interface for sequence-specific recognition. Proteases generated using this minimalist catalytic motif are designated "DP" (de novo protease).

To enable precise co-design of enzyme functionality and substrate specificity, we employed Proteus2, our generative flow-based model significantly advanced over its predecessor[39]. To explicitly endow the structural generative process with a deep understanding of substrate sequence

constraints and specificity, we integrated a customized protein language model pre-trained on UniRef50[40] with an auxiliary structural decoding objective (see Methods). Proteus2 was trained on experimental structures from the Protein Data Bank[41] and high-confidence AlphaFold2[42] predictions using a dual-modality motif scaffolding task. In this framework, sequence and structure conditions are treated as independent masking tracks, leveraging geometry-aware sequence semantics to control structure generation. This decoupled conditioning strategy empowers the model to process hybrid inputs comprising structurally defined catalytic motifs and coordinate-free substrate sequences, thereby generating metalloproteases with stabilized catalytic sites and precise substrate specificity.

We leveraged Proteus2 to co-generate metalloprotease–substrate complex structures using the extracted active motif configurations as templates. To determine the catalytically competent conformation of the substrate relative to the catalytic residues, we used AlphaFold3[43] to model the substrate peptide configuration within the template protease. The predictions revealed that the substrate adopted a β-strand conformation in both enzymes (**Extended Data Fig. 1**). From these predicted structures, we extracted the P2–P1′ backbone atoms of the Fungalysin substrate peptide (where P1 is the residue immediately preceding, and P1′ immediately following, the cleavage site), and the P3–P1 backbone atoms of the PPEP-1 substrate. In both cases, these segments form strand pairing interactions with the enzyme's strand adjacent to the active site, thereby enabling the construction of a complete target active site. To maximize structural complementarity and specificity for the substrate peptide, we developed a ‘two-step encapsulation’ strategy based on Proteus2 (**Fig. 1c,d**). Unlike conventional one-step generative approaches—which frequently yield suboptimal packing and limited control over overall enzyme topology—our method proceeds

sequentially. The first step generates the protein backbone surrounding the catalytic glutamate, stabilizing the general base and achieving partial pre-wrapping of the substrate. In the second step, the scaffold is constructed around the oxyanion hole to complete substrate peptide encapsulation. This stepwise process minimizes steric clashes, substantially enhances the packing density at the enzyme–substrate interface, and consistently generates clamp-like enzymes that precisely grasp the substrate peptide—thereby improving sequence-specific recognition. Following backbone generation, protein sequences were optimized using LigandMPNN[44], and the resulting protease–substrate–zinc complex structures were validated with AlphaFold3 to ensure convergence to the intended catalytic geometry.

De novo proteases facilitate the direct hydrolysis of Aβ peptide

We selected the amyloid-β (Aβ) peptide as the substrate for design, given its central role in Alzheimer's disease (AD) pathology, where the aggregation of neurotoxic Aβ plaques is a hallmark event[45]. The pathological self-assembly of Aβ is primarily driven by intermolecular interactions within two hydrophobic regions: the central hydrophobic core (residues 17–21) and the C-terminal segment (residues 30–42) (**Fig. 2a**). These domains act as critical nucleation sites for β-sheet stacking, facilitating the formation of stable, neurotoxic fibrils[46,47]. Consequently, these regions represent key therapeutic targets for catalytic interventions aimed at destabilizing amyloid architecture and mitigating AD progression[48]. To demonstrate the generalizability of our computational methodology, we selected three distinct cleavage sites within Aβ: one within the central hydrophobic core and two within the C-terminal hydrophogic region. We employed both the peptide-binding pocket (PP) and de novo protease (DP) strategies to design metalloproteases targeting each site. On average, 26 designs were selected from each strategy–substrate pair for

experimental characterization (**Extended Data Table 2**). These designed enzymes were expressed in *Escherichia coli*, purified using Ni-NTA magnetic beads, with the His-tag subsequently removed via HRV3C protease. Final purification was performed by size exclusion chromatography. To assess catalytic activity, we engineered fusion substrates in which the targeted Aβ fragment was inserted between the mannose-binding protein (MBP) and a small ubiquitin-like modifier (SUMO) tag. Successful proteolytic cleavage results in two lower-molecular-weight fragments, readily detectable by SDS-PAGE (**Fig. 2b**). Upon overnight incubation of the designed proteases with their respective substrates in the presence of zinc, we observed that the DP strategy yielded active enzymes for all three targeted sites: DP720-S1, DP622-S2, and DP221-S3. In contrast, the PP strategy generated active designs only for the first site, resulting in PP507-S1 and PP532-S1 (**Fig. 2c**). We attribute the limited success of the PP designs at the remaining sites to steric constraints imposed by excessive preservation of the template backbone, which may be incompatible with the sequence and geometry of these cleavage sites. In contrast, the DP strategy allows broader sampling of the conformational space, facilitating the discovery of active variants. Proteolytic specificity was confirmed by mass spectrometry analysis of the cleavage products, with observed molecular weights matching the theoretical predictions and validating site-specific cleavage (**Extended Data Fig. 2**). Notably, for DP221-S3, in addition to the major mass spectrometric peak corresponding to the intended cleavage products, a very minor peak—representing approximately 10% of the main product's abundance—was also observed, indicating an alternative cleavage site shifted by one residue toward the C-terminus (**Extended Data Fig. 2e**). We next characterized their catalytic efficiency by monitoring the time course of substrate cleavage (**Extended Data Fig. 3**). At a 1:2 enzyme-to-substrate molar ratio, DP622-S2 exhibited the highest activity, achieving complete substrate degradation within 4 hours (**Extended Data Fig. 3b**). DP720-S1 and PP507-

181 S1 achieved full digestion in 8 hours (**Extended Data Fig. 3a,c**), while PP532-S1 required nearly
182 12 hours for complete cleavage (**Extended Data Fig. 3e**). In contrast, DP221-S3 displayed slower
183 kinetics, cleaving more than half of the substrate after 12 hours (**Extended Data Fig. 3d**).
184 Collectively, these results indicate our design strategies enables the de novo generation of
185 sequence-specific metalloproteases capable of targeting disease-relevant sites within Aβ.
186

187 **Validation of catalytic mechanism**

188 To elucidate the catalytic mechanism and confirm the functional roles of key active site residues,
189 we conducted a series of site-directed mutagenesis experiments (**Fig. 3a**). For designs generated
190 by both the DP and PP strategies, the catalytic glutamate and oxyanion hole residues (histidine in
191 the DP designs and tyrosine in the PP designs) were mutated to alanine (**Fig. 3b**). Additionally, in
192 the DP designs, we mutated the newly generated second-sphere residues that form hydrogen bonds
193 with the zinc-coordinating residues, to evaluate their contribution to catalytic activity. Functional
194 assays revealed that substitution of the catalytic glutamate with alanine universally abolished
195 proteolytic activity across both DP and PP designs, highlighting its indispensable role as the
196 general base in catalysis (**Fig. 3b**). Interestingly, in the DP designs, mutation of the oxyanion hole
197 histidine to alanine had minimal or even positive effects on protease function; notably, the H191A
198 variant of DP221-S3 exhibited enhanced substrate degradation. By contrast, in the PP designs,
199 alanine substitution of the oxyanion hole tyrosine resulted in partial reduction of activity. These
200 findings suggest that the oxyanion stabilization function may be partially compensated by solvent
201 molecules in the absence of the native residue. Furthermore, mutagenesis of the second
202 coordination sphere residues in the DP designs underscored their importance in tuning catalytic
203 efficiency. The D128A mutation in DP720-S1 and the N111A mutation in DP221-S3 each resulted

204 in a marked reduction in activity. In DP622-S2, single mutations (D126A or Y91F) had minimal
205 impact on catalytic activity, whereas the double mutant (D126A/Y91F) led to a dramatic decrease
206 in activity (**Fig. 3b**). These results suggest that second-shell interactions play context-dependent
207 roles in stabilizing the primary coordination environment and modulating the electrostatic
208 landscape of the active site. Collectively, these findings support the conclusion that the observed
209 catalytic activity arises from the designed active sites and highlight the importance of precise active
210 site architecture for efficient catalysis.
211
212 **Characterization of the catalytic kinetics**
213 To quantitatively assess the kinetics of our designed proteases, we developed a specialized
214 fluorescence-based assay. The intrinsic hydrophobicity of the Aβ target sequences posed
215 significant challenges for synthesizing peptides compatible with standard fluorophore-quencher
216 systems, due to marked solubility and aggregation issues. As an alternative, we engineered a
217 FRET-based biosensor by inserting the targeted Aβ sequences directly between the fluorescent
218 protein pair mTurquoise2 (donor) and mVenus (acceptor) (**Extended Data Table 3**). In this system,
219 enzymatic cleavage of the substrate separates the fluorescent proteins, resulting in a measurable
220 decrease in FRET efficiency. Kinetic parameters were determined by fitting initial reaction
221 velocities to the Michaelis-Menten model (**Fig. 3c**). Analysis revealed that the turnover numbers
222 (k_{cat}) for our designs were generally on the order of 10^{-4} s^{-1}, with Michaelis constants (K_m) in the
223 micromolar range. These k_{cat} values represent an average > 10^7-fold rate enhancement relative to
224 the uncatalyzed hydrolysis of peptide bonds[31]. Among the designed proteases, DP622-S2
225 demonstrated the highest catalytic efficiency, achieving a k_{cat}/K_m of 160.8 $M^{-1}s^{-1}$, driven by a
226 favorable combination of a high k_{cat} (0.0009 s^{-1}) and a low K_m (5.36 μM). The PP507-S1 and

227 PP532-S1 exhibited moderate efficiencies of 28.4 and 24.3 $M^{-1}s^{-1}$, respectively, while DP221-S3
228 and DP720-S1 displayed the lowest efficiencies at 4.2 and 3.8 $M^{-1}s^{-1}$. With the exception of DP720-
229 S1, these kinetic findings were in close concordance with our time-course degradation assays. The
230 discrepancy observed for DP720-S1—which showed effective substrate degradation comparable
231 to PP507-S1 in previous assays but exhibited low catalytic efficiency in the FRET system—may
232 be attributable to steric hindrance, as the bulky fluorescent proteins could restrict substrate access
233 to the active site. Notably, the K_m value of our lead design, DP622-S2, closely parallels those of
234 naturally occurring Aβ-degrading proteases such as Insulin-Degrading Enzyme, which also exhibit
235 K_m values in the low micromolar range[49]. Although the turnover rates of our designs are lower than
236 those of natural enzymes, achieving micromolar substrate affinity demonstrates that our
237 computational strategy can successfully encode robust recognition for disease-relevant targets.
238
239 To further elucidate the functional roles of the oxyanion hole and second coordination sphere
240 residues, we characterized the catalytic kinetics of the corresponding mutants, including single
241 mutants of DP622-S2 (Y91F, D126A, or H172A), DP221-S3 (H191A), as well as the DP622-S2
242 double mutant (Y91F/D126A) (**Extended Data Fig. 4**). Intriguingly, all tested single mutations in
243 the DP622-S2 series (Y91F, D126A, and H172A) (**Extended Data Fig. 4a-c**) showed enhanced
244 catalytic efficiency (k_{cat}/K_m) compared to the parental design, whereas the double mutant
245 Y91F/D126A decreased catalytic efficiency (**Extended Data Fig. 4d**), consistent with the SDS-
246 PAGE results. The observed improvements were predominantly driven by increased turnover
247 numbers (k_{cat}); notably, the DP622-S2 D126A variant exhibited a threefold increase in k_{cat}
248 (**Extended Data Fig. 4b**). This suggests that optimizing the catalytic microenvironment can
249 significantly modulate the activation energy barrier of the rate-limiting step. Most mutations led

250 to a modest decrease in substrate affinity, as reflected by an increase in K_m; however, the DP622-
251 S2 Y91F variant maintained a K_m nearly identical to the original, resulting in a twofold
252 enhancement in overall catalytic efficiency **(Extended Data Fig. 4a)**. The DP221-S3 H191A
253 mutation had a synergistic effect, increasing k_{cat} while simultaneously decreasing K_m, resulting in
254 a 2.7-fold improvement in catalytic efficiency **(Extended Data Fig. 4e)**. Together, these findings
255 indicate that second-shell coordination and oxyanion hole residues have a substantial impact on
256 catalytic efficiency, largely by modulating k_{cat}—a parameter that remains challenging to accurately
257 model in current design protocols.
258
259 **Characterization the substrate specificity**
260 We next assessed the substrate specificity of the designed metalloproteases by evaluating their
261 cleavage activity against three distinct MBP–Aβ_segment–SUMO fusion constructs (Substrates 1,
262 2, and 3) (**Fig. 4**). SDS-PAGE analysis of the cleavaged products revealed that PP507-S1 exhibited
263 the highest degree of selectivity, catalyzing cleavage exclusively of Substrate 1, with no detectable
264 activity against the other two substrates (**Fig. 4b**). In contrast, PP532-S1 displayed broader
265 substrate tolerance, efficiently processing all three substrates (**Fig. 4c**), while PP720-S1 showed
266 measurable, though reduced, activity against Substrate 2 (**Fig. 4a**). DP622-S2 and DP221-S3
267 exhibited partial cross-reactivity with each other's substrates, albeit at considerably lower
268 efficiencies compared to their cognate targets (**Fig. 4d,e**). We speculate that the observed cross-
269 reactivity for DP622-S2 and DP221-S3 may be attributed to extensive sequence overlap between
270 the target sequences and the use of glycine-serine (GS) linkers flanking the inserted Aβ segments,
271 which may facilitate recognition of similar sequence motifs across different constructs (**Extended**
272 **Data Table 1**). Notably, the flanking sequence of the S1 cleavage site contains a high proportion

273 of bulky aromatic and large hydrophilic residues, whereas the regions flanking the S2 and S3 sites
274 are primarily composed of small aliphatic amino acids and glycines. This composition may
275 underlie the high specificity of PP507 and likely prevents the S2/S3 enzymes from cleaving the
276 S1 substrate due to steric occlusion.
277
278 We next evaluated the substrate specificity of the active site mutants (**Extended Data Fig. 5**). The
279 second-shell and oxyanion hole mutants in DP622 and DP720 exhibited specificity profiles similar
280 to those of their respective parent designs (**Extended Data Fig. 5a,b**). Notably, the DP221-S3
281 H191A variant showed a remarkable increase in selectivity, virtually abolishing cleavage activity
282 toward non-target substrates (**Extended Data Fig. 5c**). However, mass spectrometry analysis of
283 the cleavage products revealed that the scissile bond shifted almost entirely to the original minor
284 cleavage site—one residue closer to the C-terminus—compared to the parent design (**Extended**
285 **Data Fig. 6b**). In contrast, the DP622-S2 Y91F mutant retained the intended cleavage site,
286 consistent with the parental enzyme (**Extended Data Fig. 6a**). Nonetheless, the stringent
287 specificity demonstrated by PP507-S1 underscores the potential of our approach to generate
288 custom, sequence-specific proteases. We anticipate that future iterations incorporating explicit
289 negative design strategies during the design and filtering stages will further enhance substrate
290 specificity.
291
292
293 To further evaluate the cleavage activity of our most effective designs and select variants—
294 including PP507, DP622 Y91F, and DP221 H191A, we incubated all three enzymes together with
295 a full-length synthetic Aβ42 peptide. Mass spectrometry analysis revealed a diverse mixture of

296 peptide species. Notably, alongside with several partially cleaved intermediate fragments, we
297 successfully detected the expected fully cleaved products (DAEFRHDSGYEVHHQKL,
298 VFFAEDVGSNKGAIIGL, and VVIA) (**Extended Data Fig. 7**). These results confirm that our de
299 novo metalloproteases are capable of catalyzing the site-specific hydrolysis of the full-length Aβ42
300 peptide as designed.
301
302 **Structural characterization of the protease-substrate complex**
303 To assess the structural accuracy of our computational models, we determined the cryo-EM
304 structures of PP507-S1, DP622-S2, and DP221-S3 in complex with the Aβ42 peptide (**Fig. 5a**). To
305 overcome the resolution limitations inherent to the small molecular weight of the designed
306 proteases, each protease was rigidly fused with a large helical bundle protein generated by Proteus2
307 (**Extended Data Fig. 8**). Minimal interfacial interactions were computationally introduced to
308 rigidify the fusion construct, ensuring that neither the overall fold nor the active site architecture
309 of the protease was perturbed. To capture the pre-catalytic Aβ42-bound state, the catalytic
310 glutamate in each protease was mutated to glutamine (E to Q). The resulting fusion proteins, with
311 inactivated active sites, were incubated with the Aβ42 peptide and subjected to cryo-EM structure
312 determination (**Extended Data Fig. 9**). Focused refinement of the protease region within the
313 fusion protein yielded structures at resolutions ranging from 2.98 to 3.44 Å (**Extended Data Fig.
314 10**). The reconstructions revealed clear, continuous density for the Aβ42 substrate, allowing
315 confident assignment of the peptide backbone and local side chains within the binding cleft (**Fig.
316 5b**). The resolved peptide sequence confirms that all three proteases specifically recognize the
317 designed Aβ segment, consistent with their high substrate specificity.
318

Superimposing the experimentally determined cryo-EM structures onto their respective computational models revealed a high degree of global structural agreement, with Cα root-mean-square deviation (RMSD) values ranging from 1.13 to 1.88 Å. This high structural fidelity underscores the robustness of our flow-based generative strategy in accurately constructing the overall protein structures (**Fig. 5c**). Furthermore, detailed inspection of the superimposed active sites confirmed that the designed catalytic geometries were accurately recapitulated in the experimental structures (**Fig. 5d**). Critical spatial arrangements were evaluated by measuring the distances between the substrate P1 backbone carbonyl oxygen, the coordinating zinc ion, and the designed oxyanion hole residue. In PP507-S1 and DP221-S3, we observed local structural relaxation within the binding pocket. For PP507-S1, the P1 oxygen–zinc distance expanded to 5.1 Å in the cryo-EM structure compared to the designed 2.1 Å, and its distance to the tyrosine oxyanion hole increased from 2.7 Å to 4.4 Å. Similarly, DP221-S3 exhibited an enlarged P1 oxygen–zinc distance of 3.2 Å (designed 2.3 Å) and a relaxed distance of 4.4 Å to the histidine oxyanion hole (designed 2.1 Å). In contrast, the active site of DP622-S2 demonstrated remarkable structural fidelity, maintaining a tightly coordinated P1 oxygen–zinc distance of 2.3 Å (closely matching the designed 2.1 Å) and faithfully preserving the designed 2.8 Å distance to the histidine oxyanion hole. The precise geometric pre-organization of the DP622-S2 active site is consistent with our kinetic observations (**Fig. 3c**), which demonstrate both higher substrate affinity and a moderately improved turnover rate for DP622-S2 compared to PP507-S1 and DP221-S3. Collectively, these structural insights, together with biochemical data, underscore that achieving high precision in active site geometry remains critical for enhancing the efficiency of de novo designed enzymes.

342 **Discussion**

343 By explicitly integrating target sequence information into the flow-based structure generation
344 process, Proteus2 enables the direct generation of sequence-specific metalloproteases. Our two-
345 step encapsulation strategy facilitates the creation of clamp-like proteases that envelop the
346 substrate peptide, thereby maximizing both specificity and discrimination. The successful design
347 of metalloproteases capable of cleaving three distinct native Aβ peptide sequences extends de novo
348 protein design beyond stable binding, enabling functional proteolysis of physiological targets. The
349 atomic-level agreement between the design models and experimentally determined protease-
350 substrate complex structures further demonstrates that our computational approach can achieve
351 both high structure accuracy and precise substrate discrimination. Our specificity characterization
352 also indicates that, for future enzyme design, careful selection of the target site is critical; regions
353 enriched in distinctive side chains, such as bulky aromatic or highly charged residues, may
354 facilitate the development of enzymes with higher specificity. While a certain degree of
355 nonspecific cleavage was seen in some designes, the clamp-like architecture provides a robust
356 starting point for further sequence redesign or structure-guided refinement to enhance specificity.
357

358 Our successful de novo design of metalloproteases, starting from minimalist catalytic motifs,
359 represents a major advance in the de novo enzyme design field by bridging the gap between model
360 reactions and catalysis relevant for therapeutic intervention. On average, our designs accelerate
361 peptide bond cleavage by more than 10^7-fold compared to the uncatalyzed reaction in aqueous
362 solution[31]. Importantly, these metalloproteases exhibit substrate affinities (K_m) comparable to those
363 of natural enzymes, indicating that our design strategies can accommodate the structural and
364 chemical complexity of physiological polypeptides[49]. However, our mutational analysis also

365 indicates that key microenvironmental factors affecting turnover rates (k_{cat}) remain challenging to
366 accurately model with current approach. While our structural characterization indicates that
367 improving the modeling precision of the active site might represent a promising direction for
368 enhancing catalytic efficiency, further advancements will necessitate careful consideration of
369 solvent effects, second-shell coordination, and the dynamic nature of the catalytic process to
370 achieve optimal catalytic proficiency.
371
372 The aggregation of Aβ into neurotoxic plaques is a defining event in Alzheimer's disease (AD)
373 pathology, making the development of molecular tools to counteract Aβ accumulation a high
374 priority. Current strategies for Aβ clearance, predominantly based on monoclonal antibodies[50], act
375 by sequestering Aβ for immune-mediated removal rather than direct peptide degradation[51]. In
376 contrast, catalytic degradation offers a compelling alternative, as a single enzyme can process
377 multiple Aβ molecules through direct hydrolysis. Although endogenous proteases like neprilysin
378 and insulin-degrading enzyme can target Aβ[52,53], their broad specificity presents a risk for
379 undesirable off-target effects when therapeutically enhanced[54,55]. Our work provides a
380 fundamentally distinct strategy—fully de novo design of programmable, sequence-specific
381 proteases for Aβ peptide degradation—enabling the selective hydrolysis of pathogenic sequences
382 and facilitating efficient monomer clearance. By targeting cleavage within the hydrophobic,
383 aggregation-prone regions of Aβ, these proteases have the potential to inhibit the formation of
384 toxic fibrils. Notably, the cleavage site for our most specific design, PP507-S1, is only one residue
385 away from the α-secretase site responsible for the non-pathogenic processing of APP, showcasing
386 the potential for precision engineering[56]. As de novo designed enzymes can target different sites,

our multi-enzyme cocktail approach may reveal new possibilities for developing therapeutic interventions for AD.

Overall, our work establishes a robust and generalizable framework for the de novo design of programmable, sequence-specific metalloproteases with wide-ranging applications in research and medicine. Our design approach can be readily adapted to other protease classes, such as serine or cysteine proteases, opening new possibilities for selective protein manipulation and targeted protein degradation that are unattainable with naturally occurring enzymes. Looking ahead, the integration of explicit negative design strategies, machine learning-guided optimization, and advanced transition-state modeling will likely yield next-generation proteases with even higher specificity and catalytic efficiency. Ultimately, this technology sets the stage for the rational development of “designer” proteases for a broad spectrum of diseases and empowers both basic research and therapeutic innovation by providing unprecedented control over protein function in living systems.

Data availability

The density maps and structure files have been deposited into the Electron Microscopy Data Bank and the RCSB Protein Data Bank with the following accession codes: EMD-69321 and 23WM (PP507 E110Q); EMD-69322 and 23WN (DP622 E96Q); EMD-69323 and 23WO (DP221 E85Q).

Code availability

The Rosetta macromolecular modelling suite (https://www.rosettacommons.org) is freely available to academic and commercial users. Design protocols and analysis scripts used in this paper are available in the Methods and at https://github.com/LongxingLab/metalloprotease. The code for Proteus2 is currently uploaded to Zenodo at xxx.

Acknowledgements

We extend our sincere thanks to the Dang Lab at Westlake University for their valuable guidance and technical expertise in peptide synthesis. We would like to thank the Mass Spectrometry Facility of Westlake University for help in sample analysis; and the Westlake University HPC Center for computation assistance.

Author contributions

Y.Q., C.W. and L.C. designed the research. Y.Q., C.W. and L.C. developed the design pipeline and made the designs. Y.Q., H.Z. and Y.W. pefromed the experiments. All authors analysed data. L.C. supervised research. Y.Q., C.W. and L.C. wrote the manuscript with the input from the other authors. All authors revised the manuscript.

Competiting interests

A provisional patent application will be filed prior to publication.

Funding sources

This work was supported by grants from the National Key R&D Program of China (2022YFA1303700), the National Natural Science Foundation of China (32370989, 3257120243), The Zhejiang Province Pioneer Plan (2025C01189), and Westlake Education Foundation to L.C.

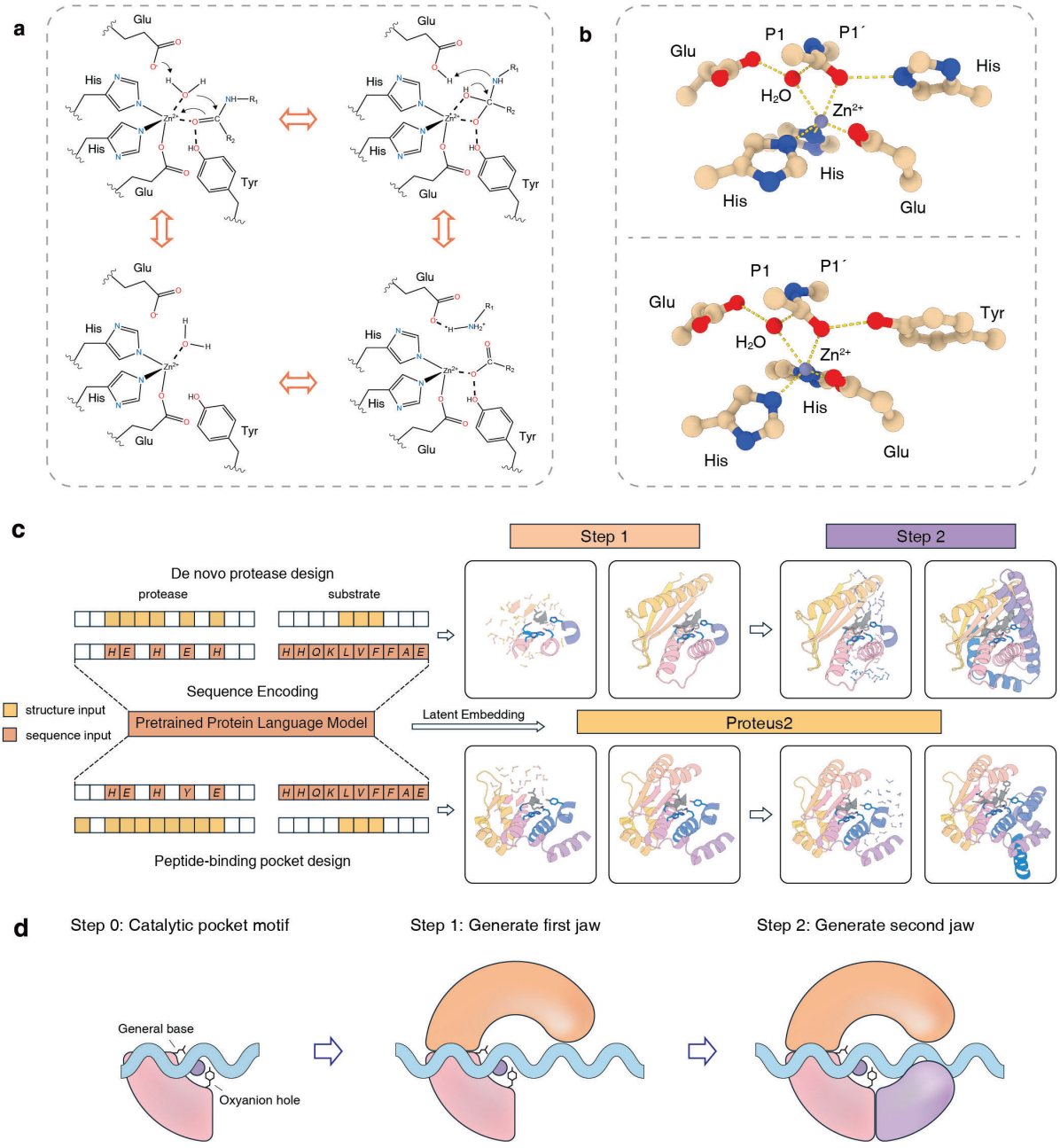

Fig. 1: Catalytic mechanism of zinc-dependent metalloproteases and two-step de novo design of clamp-like protease scaffolds. a, The catalytic cycle of zinc-dependent metalloproteases involves a precisely orchestrated sequence of molecular events at the active site. The reaction

initiates as the scissile carbonyl oxygen of the substrate coordinates with the catalytic zinc ion, polarizing the carbonyl and increasing its electrophilicity. Concurrently, a conserved glutamate residue acts as a general base, deprotonating a zinc-bound water molecule to trigger nucleophilic attack on the carbonyl carbon. This generates a transient tetrahedral intermediate, with its negatively charged oxyanion stabilized via hydrogen bonds within the oxyanion hole—typically formed by a tyrosine or histidine. The catalytic glutamate then functions as a general acid, transferring a proton to the amide nitrogen of the leaving group, thereby facilitating intermediate collapse and peptide bond cleavage. The hydrolyzed products subsequently dissociate, and a new water molecule occupies the zinc coordination sphere, restoring the enzyme for further catalytic cycles. **b,** Theozyme models for the Zn(II)-activated water nucleophilic attack on the substrate peptide bond. Both panels illustrate the core catalytic components: the central Zn(II) ion coordinated by three endogenous amino acid residues, the catalytic glutamate acting as a general base, the nucleophilic water molecule, and the substrate scissile bond represented by the P1 and P1' residues. **c**, Computational framework for designing substrate-specific metalloproteases. Generation is initialized with either a minimalist catalytic motif (de novo design) or a largely preserved template topology (pocket design). A pretrained protein language model encodes the sequences of the substrate and catalytic residues into latent embeddings. These embeddings, alongside the structural motif, condition the Proteus2 generative model for substrate-sequence-aware protease design via a two-step encapsulation strategy. **d**, Schematic representation of the two-step encapsulation strategy. The scaffold is assembled in a sequential manner to achieve complete substrate encapsulation, ensuring that the clamp precisely engages the target peptide for sequence-specific recognition.

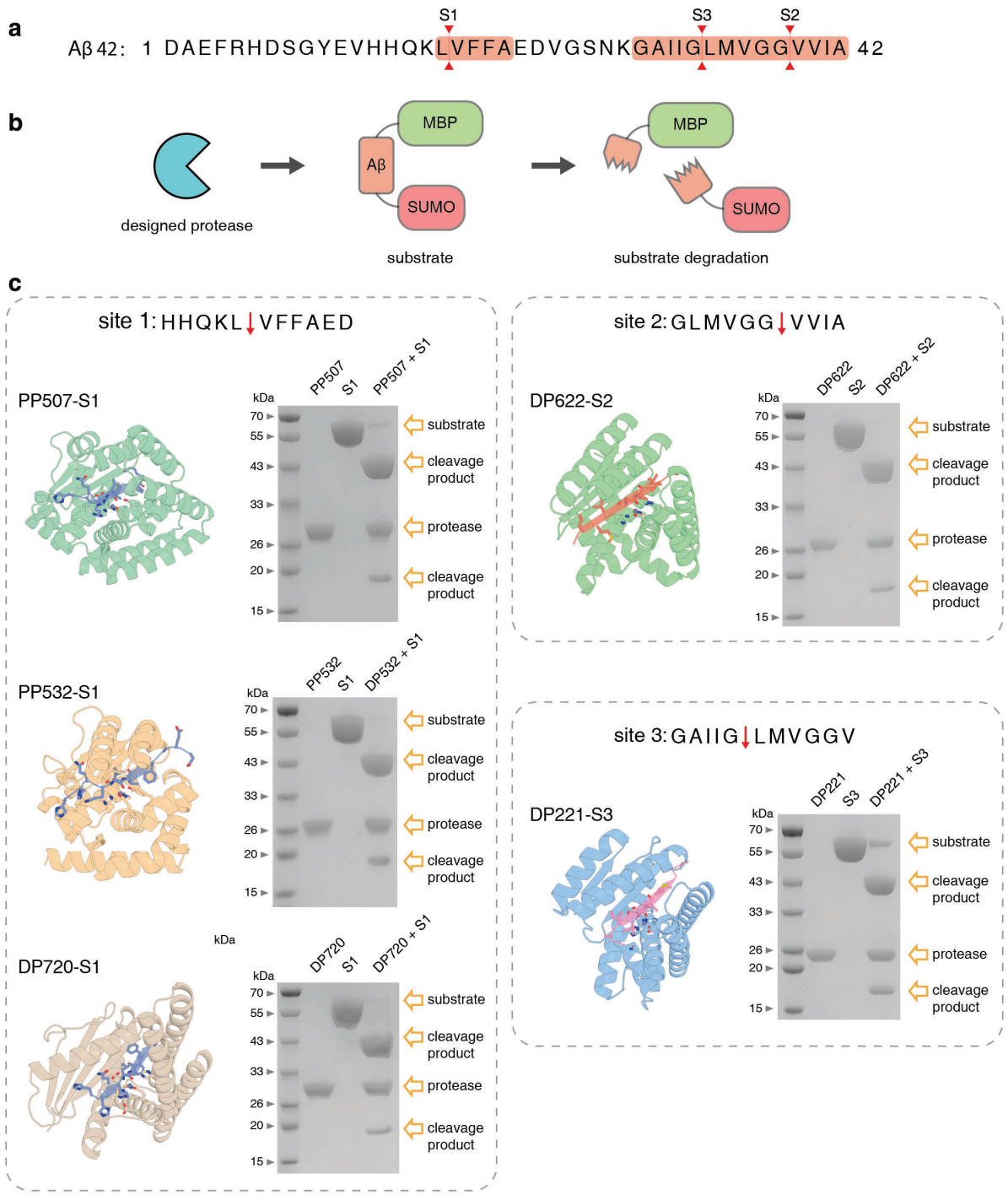

454

455 **Fig. 2: Experimental validation of designed metalloproteases targeting Aβ. a**, Primary
456 sequence of Aβ42. The complete amino acid sequence of Aβ42 is shown, with two main
457 hydrophobic domains highlighted in orange and three selected cleavage sites marked in red. **b**,

Schematic of the proteolysis assay. To facilitate expression and protelytic analysis, Aβ segment was engineered as a fusion protein (MBP-Aβ_segment-SUMO). The diagram illustrates that specific cleavage within the Aβ sequence by the designed proteases results in separation of the MBP and SUMO fragments, which are readily detected via molecular weight shifts in SDS-PAGE experiments. **c**, Design models and proteolytic screening of designed proteases. Design models of five designed proteases are displayed alongside SDS-PAGE analysis, which confirms the successful cleavage of the MBP-Aβ-SUMO substrate.

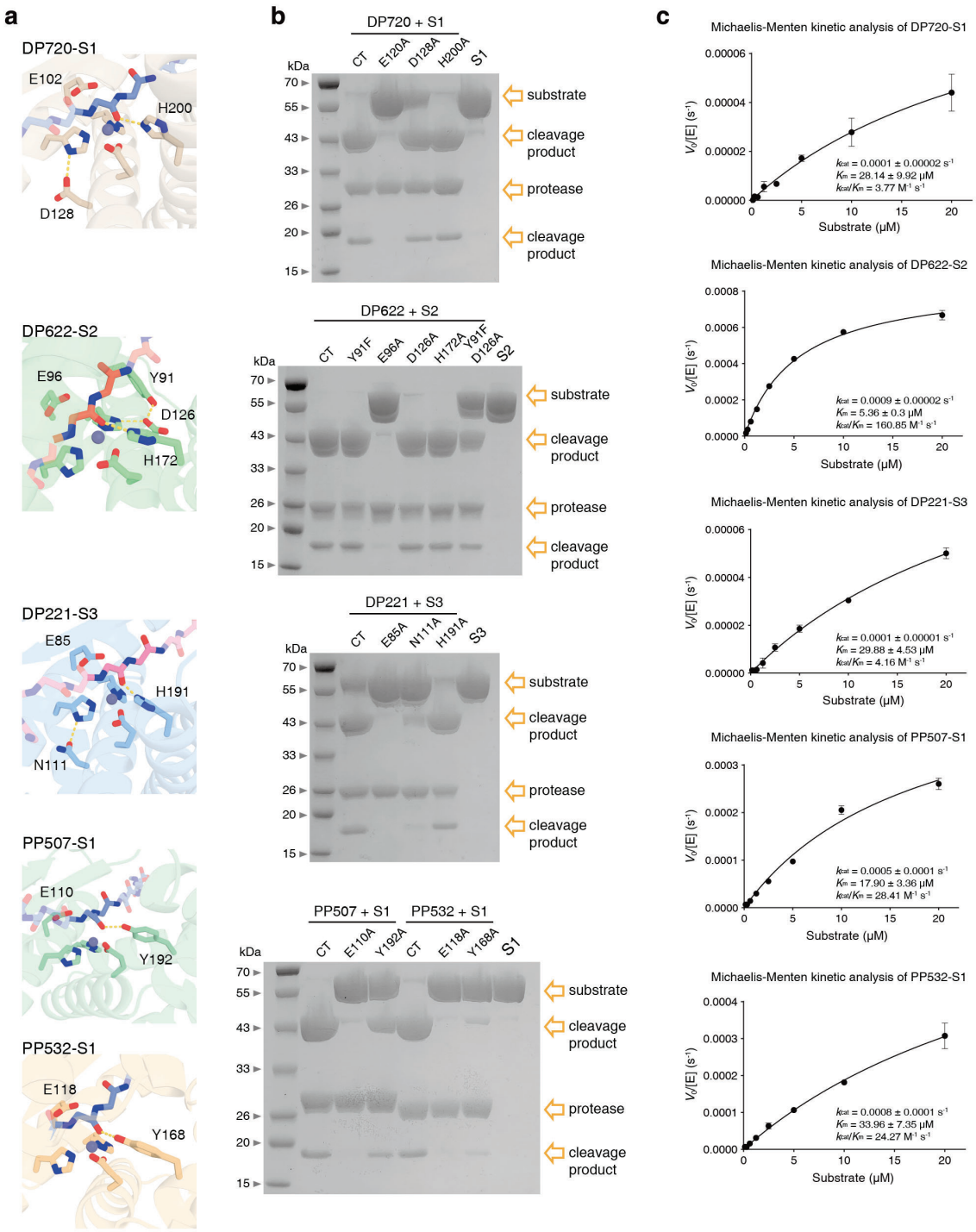

Fig. 3: Mutagenesis and kinetic characterization of the designed metalloproteases. a, Atomic details of the active site architectures in the design models, highlighting the precise spatial arrangement of key catalytic residues. The coordination of the zinc ion by histidines and

470 glutamates, the positioning of the general base, and the configuration of the oxyanion hole are
471 illustrated. **b,** Mutational analysis of catalytic residues. SDS-PAGE analysis of various catalytic
472 residue mutants is shown, verifying the functional roles of the designed active site residues. **c,**
473 Kinetic characterization of the designed proteases. Proteolytic kinetics were assessed by measuring
474 initial reaction velocities at varying substrate concentrations. Data were fitted to the Michaelis-
475 Menten equation to determine key kinetic parameters, including the Michaelis constant (K_m) and
476 turnover number (k_{cat}). The calculated k_{cat}/K_m values quantify the catalytic efficiency of the de
477 novo designed enzymes, demonstrating their substrate recognition and cleavage ability. Data
478 represent mean ± standard deviation (black dots and error bars).
479

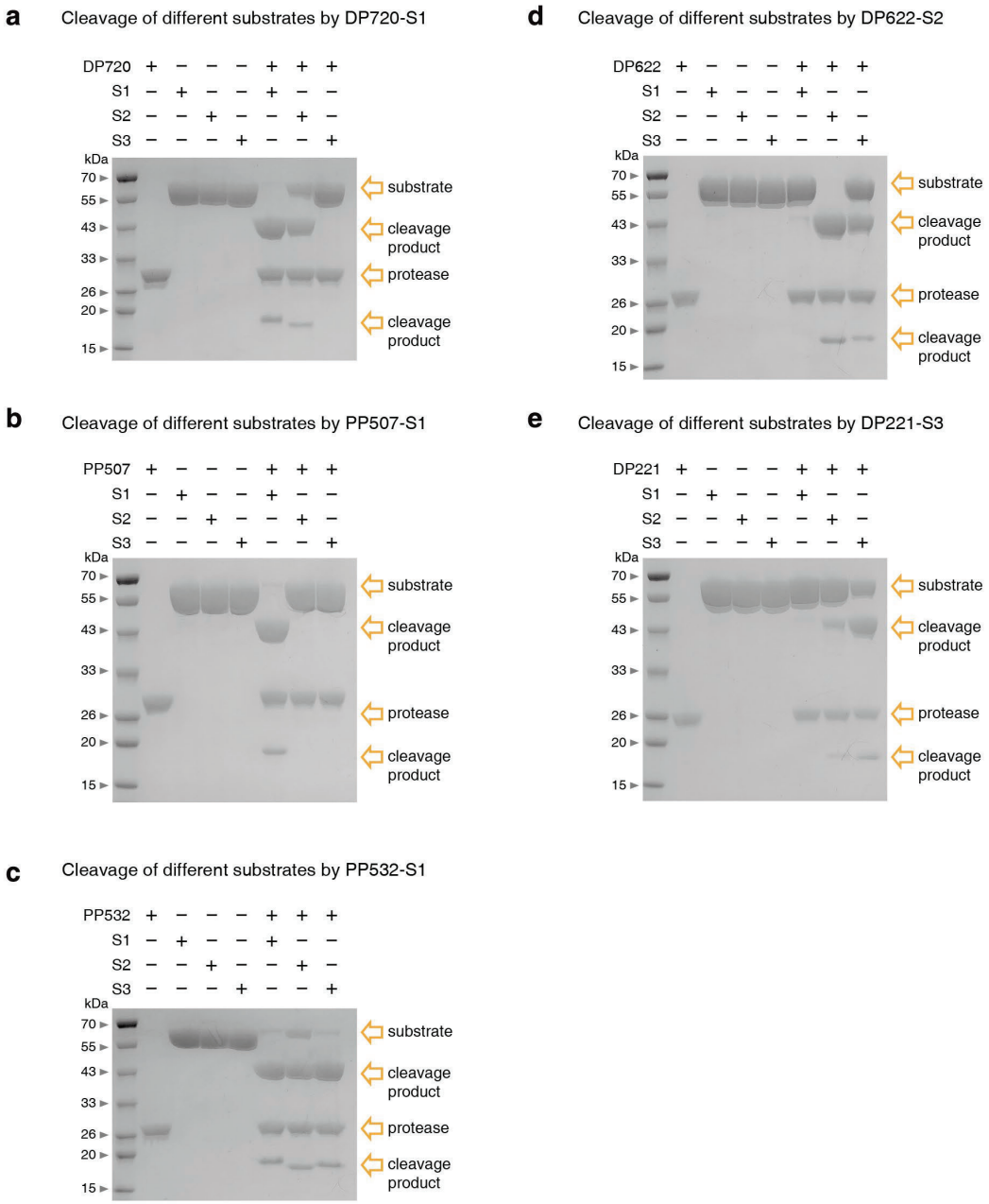

Fig. 4: Proteolytic specificity and substrate selectivity of designed proteases. The substrate recognition profiles of five designed proteases (**a**, DP720-S1; **b**, PP507-S1; **c**, PP532-S1; **d**, DP622-S2; **e**, DP221-S3) were systematically evaluated using the three structurally distinct MBP-

484 Aβ_segment-SUMO fusion constructs (Substrates 1, 2, and 3). The results demonstrate the
485 sequence and site selectivity of each protease toward their corresponding substrates.

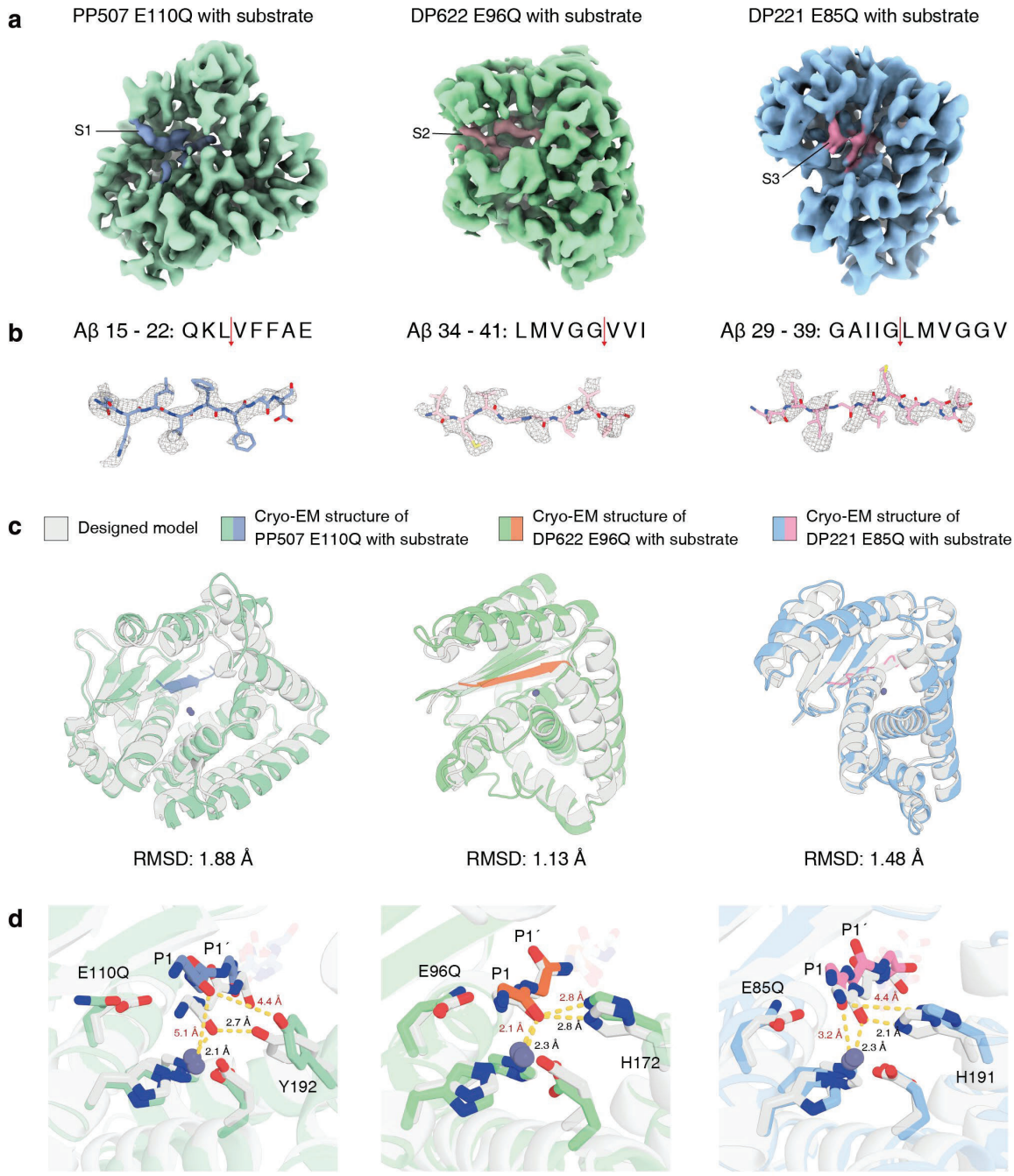

Fig. 5: Cryo-EM structure characterization of designed protease in complex with Aβ42. a, Overall cryo-EM density maps for each of the three designed proteases. To capture the pre-catalytic substrate-bound complex, the catalytic glutamate in each design was mutated to

490 glutamine (E to Q). **b,** Local cryo-EM density maps highlighting the bound Aβ42 substrate. **c,**
491 Superimposition of the computational design models (grey) and the experimentally determined
492 cryo-EM structures (colored), with backbone Cα RMSD values indicated. **d,** Close-up views of
493 the superimposed active sites. Key catalytic geometries are assessed by measuring the distances
494 between the substrate P1 backbone carbonyl oxygen, the designed oxyanion hole residue, and the
495 catalytic zinc ion. Distance labels are shown in black for the design models and in red for the cryo-
496 EM structures.
497

Reference

1 Lopez-Otin, C. & Bond, J. S. Proteases: multifunctional enzymes in life and disease. *J Biol Chem* **283**, 30433-30437 (2008). https://doi.org:10.1074/jbc.R800035200

2 Taylor, R. C., Cullen, S. P. & Martin, S. J. Apoptosis: controlled demolition at the cellular level. *Nat Rev Mol Cell Biol* **9**, 231-241 (2008). https://doi.org:10.1038/nrm2312

3 Seidah, N. G. & Prat, A. The biology and therapeutic targeting of the proprotein convertases. *Nat Rev Drug Discov* **11**, 367-383 (2012). https://doi.org:10.1038/nrd3699

4 Turk, B. Targeting proteases: successes, failures and future prospects. *Nat Rev Drug Discov* **5**, 785-799 (2006). https://doi.org:10.1038/nrd2092

5 Bonnans, C., Chou, J. & Werb, Z. Remodelling the extracellular matrix in development and disease. *Nat Rev Mol Cell Biol* **15**, 786-801 (2014). https://doi.org:10.1038/nrm3904

6 Kirk, O., Borchert, T. V. & Fuglsang, C. C. Industrial enzyme applications. *Curr Opin Biotechnol* **13**, 345-351 (2002). https://doi.org:10.1016/s0958-1669(02)00328-2

7 Li, Q., Yi, L., Marek, P. & Iverson, B. L. Commercial proteases: present and future. *FEBS Lett* **587**, 1155-1163 (2013). https://doi.org:10.1016/j.febslet.2012.12.019

8 Perona, J. J. & Craik, C. S. Evolutionary divergence of substrate specificity within the chymotrypsin-like serine protease fold. *J Biol Chem* **272**, 29987-29990 (1997). https://doi.org:10.1074/jbc.272.48.29987

9 Hedstrom, L. Serine protease mechanism and specificity. *Chem Rev* **102**, 4501-4524 (2002). https://doi.org:10.1021/cr000033x

10 Craik, C. S., Page, M. J. & Madison, E. L. Proteases as therapeutics. *Biochem J* **435**, 1-16 (2011). https://doi.org:10.1042/BJ20100965

11 Dyer, R. P. & Weiss, G. A. Making the cut with protease engineering. *Cell Chem Biol* **29**, 177-190 (2022). https://doi.org:10.1016/j.chembiol.2021.12.001

12 Blum, T. R. *et al.* Phage-assisted evolution of botulinum neurotoxin proteases with reprogrammed specificity. *Science* **371**, 803-810 (2021). https://doi.org:10.1126/science.abf5972

13 Gao, Z. *et al.* A gasdermin-based life-death evolution system for reprogramming protease specificity. *Nat Chem Biol* (2025). https://doi.org:10.1038/s41589-025-02063-3

14 Dyer, R. P. *et al.* Reengineering the specificity of the highly selective Clostridium botulinum protease via directed evolution. *Sci Rep* **12**, 9956 (2022). https://doi.org:10.1038/s41598-022-13617-z

15 Bode, W., Gomis-Ruth, F. X. & Stockler, W. Astacins, serralysins, snake venom and matrix metalloproteinases exhibit identical zinc-binding environments (HEXXHXXGXXH and Met-turn) and topologies and should be grouped into a common family, the 'metzincins'. *FEBS Lett* **331**, 134-140 (1993). https://doi.org:10.1016/0014-5793(93)80312-i

16 Visse, R. & Nagase, H. Matrix metalloproteinases and tissue inhibitors of metalloproteinases: structure, function, and biochemistry. *Circ Res* **92**, 827-839 (2003). https://doi.org:10.1161/01.RES.0000070112.80711.3D

17 Spyroulias, G. A., Galanis, A. S., Pairas, G., Manessi-Zoupa, E. & Cordopatis, P. Structural features of angiotensin-I converting enzyme catalytic sites: conformational studies in solution, homology models and comparison with other zinc metallopeptidases. *Curr Top Med Chem* **4**, 403-429 (2004). https://doi.org:10.2174/1568026043451294

18 Nagase, H. & Woessner, J. F., Jr. Matrix metalloproteinases. *J Biol Chem* **274**, 21491-21494 (1999). https://doi.org:10.1074/jbc.274.31.21491
19 Blobel, C. P. ADAMs: key components in EGFR signalling and development. *Nat Rev Mol Cell Biol* **6**, 32-43 (2005). https://doi.org:10.1038/nrm1548
20 Bond, J. S. & Beynon, R. J. The astacin family of metalloendopeptidases. *Protein Sci* **4**, 1247-1261 (1995). https://doi.org:10.1002/pro.5560040701
21 Tronrud, D. E., Roderick, S. L. & Matthews, B. W. Structural basis for the action of thermolysin. *Matrix Suppl* **1**, 107-111 (1992).
22 Miyoshi, S. Extracellular proteolytic enzymes produced by human pathogenic vibrio species. *Front Microbiol* **4**, 339 (2013). https://doi.org:10.3389/fmicb.2013.00339
23 Varadarajan, N., Rodriguez, S., Hwang, B. Y., Georgiou, G. & Iverson, B. L. Highly active and selective endopeptidases with programmed substrate specificities. *Nat Chem Biol* **4**, 290-294 (2008). https://doi.org:10.1038/nchembio.80
24 Vandenbroucke, R. E. & Libert, C. Is there new hope for therapeutic matrix metalloproteinase inhibition? *Nat Rev Drug Discov* **13**, 904-927 (2014). https://doi.org:10.1038/nrd4390
25 Yeh, A. H. *et al.* De novo design of luciferases using deep learning. *Nature* **614**, 774-780 (2023). https://doi.org:10.1038/s41586-023-05696-3
26 Ahern, W. *et al.* Atom-level enzyme active site scaffolding using RFdiffusion2. *Nat Methods* (2025). https://doi.org:10.1038/s41592-025-02975-x
27 Braun, M. *et al.* Computational enzyme design by catalytic motif scaffolding. *Nature* (2025). https://doi.org:10.1038/s41586-025-09747-9
28 Kim, D. *et al.* Computational design of metallohydrolases. *Nature* (2025). https://doi.org:10.1038/s41586-025-09746-w
29 Listov, D. *et al.* Complete computational design of high-efficiency Kemp elimination enzymes. *Nature* **643**, 1421-1427 (2025). https://doi.org:10.1038/s41586-025-09136-2
30 Studer, S. *et al.* Evolution of a highly active and enantiospecific metalloenzyme from short peptides. *Science* **362**, 1285-1288 (2018). https://doi.org:10.1126/science.aau3744
31 Radzicka, A. & Wolfenden, R. Rates of Uncatalyzed Peptide Bond Hydrolysis in Neutral Solution and the Transition State Affinities of Proteases. *Journal of the American Chemical Society* **118**, 6105-6109 (1996). https://doi.org:10.1021/ja954077c
32 Kiss, G., Celebi-Olcum, N., Moretti, R., Baker, D. & Houk, K. N. Computational enzyme design. *Angew Chem Int Ed Engl* **52**, 5700-5725 (2013). https://doi.org:10.1002/anie.201204077
33 Tokuriki, N. & Tawfik, D. S. Stability effects of mutations and protein evolvability. *Curr Opin Struct Biol* **19**, 596-604 (2009). https://doi.org:10.1016/j.sbi.2009.08.003
34 Nestl, B. M. & Hauer, B. Engineering of Flexible Loops in Enzymes. *ACS Catalysis* **4**, 3201-3211 (2014). https://doi.org:10.1021/cs500325p
35 Barrozo, A., Borstnar, R., Marloie, G. & Kamerlin, S. C. Computational protein engineering: bridging the gap between rational design and laboratory evolution. *Int J Mol Sci* **13**, 12428-12460 (2012). https://doi.org:10.3390/ijms131012428
36 Chen, C. Y., Georgiev, I., Anderson, A. C. & Donald, B. R. Computational structure-based redesign of enzyme activity. *Proc Natl Acad Sci U S A* **106**, 3764-3769 (2009). https://doi.org:10.1073/pnas.0900266106

37 Pichlo, C. *et al.* Molecular determinants of the mechanism and substrate specificity of Clostridium difficile proline-proline endopeptidase-1. *J Biol Chem* **294**, 11525-11535 (2019). https://doi.org:10.1074/jbc.RA119.009029

38 Fernandez, D., Russi, S., Vendrell, J., Monod, M. & Pallares, I. A functional and structural study of the major metalloprotease secreted by the pathogenic fungus Aspergillus fumigatus. *Acta Crystallogr D Biol Crystallogr* **69**, 1946-1957 (2013). https://doi.org:10.1107/S0907444913017642

39 Wang, C. *et al.* in *Proceedings of the 41st International Conference on Machine Learning* Vol. 235 (eds Salakhutdinov Ruslan *et al.*) 51376--51395 (PMLR, Proceedings of Machine Learning Research, 2024).

40 Suzek, B. E. *et al.* UniRef clusters: a comprehensive and scalable alternative for improving sequence similarity searches. *Bioinformatics* **31**, 926-932 (2014). https://doi.org:10.1093/bioinformatics/btu739

41 Berman, H. M. *et al.* The Protein Data Bank. *Nucleic Acids Res* **28**, 235-242 (2000). https://doi.org:10.1093/nar/28.1.235

42 Jumper, J. *et al.* Highly accurate protein structure prediction with AlphaFold. *Nature* **596**, 583-589 (2021). https://doi.org:10.1038/s41586-021-03819-2

43 Abramson, J. *et al.* Accurate structure prediction of biomolecular interactions with AlphaFold 3. *Nature* **630**, 493-500 (2024). https://doi.org:10.1038/s41586-024-07487-w

44 Dauparas, J. *et al.* Atomic context-conditioned protein sequence design using LigandMPNN. *Nat Methods* **22**, 717-723 (2025). https://doi.org:10.1038/s41592-025-02626-1

45 Selkoe, D. J. & Hardy, J. The amyloid hypothesis of Alzheimer's disease at 25 years. *EMBO Mol Med* **8**, 595-608 (2016). https://doi.org:10.15252/emmm.201606210

46 Tjernberg, L. O. *et al.* Arrest of beta-amyloid fibril formation by a pentapeptide ligand. *J Biol Chem* **271**, 8545-8548 (1996). https://doi.org:10.1074/jbc.271.15.8545

47 Jarrett, J. T., Berger, E. P. & Lansbury, P. T., Jr. The carboxy terminus of the beta amyloid protein is critical for the seeding of amyloid formation: implications for the pathogenesis of Alzheimer's disease. *Biochemistry* **32**, 4693-4697 (1993). https://doi.org:10.1021/bi00069a001

48 Saido, T. & Leissring, M. A. Proteolytic degradation of amyloid beta-protein. *Cold Spring Harb Perspect Med* **2**, a006379 (2012). https://doi.org:10.1101/cshperspect.a006379

49 Mukherjee, A. *et al.* Insulysin hydrolyzes amyloid beta peptides to products that are neither neurotoxic nor deposit on amyloid plaques. *J Neurosci* **20**, 8745-8749 (2000). https://doi.org:10.1523/JNEUROSCI.20-23-08745.2000

50 van Dyck, C. H. *et al.* Lecanemab in Early Alzheimer's Disease. *N Engl J Med* **388**, 9-21 (2023). https://doi.org:10.1056/NEJMoa2212948

51 Sevigny, J. *et al.* The antibody aducanumab reduces Abeta plaques in Alzheimer's disease. *Nature* **537**, 50-56 (2016). https://doi.org:10.1038/nature19323

52 Qiu, W. Q. *et al.* Insulin-degrading enzyme regulates extracellular levels of amyloid beta-protein by degradation. *J Biol Chem* **273**, 32730-32738 (1998). https://doi.org:10.1074/jbc.273.49.32730

53 Iwata, N. *et al.* Metabolic regulation of brain Abeta by neprilysin. *Science* **292**, 1550-1552 (2001). https://doi.org:10.1126/science.1059946

54 Tang, W. J. Targeting Insulin-Degrading Enzyme to Treat Type 2 Diabetes Mellitus. *Trends Endocrinol Metab* **27**, 24-34 (2016). https://doi.org:10.1016/j.tem.2015.11.003

55 Turner, A. J., Isaac, R. E. & Coates, D. The neprilysin (NEP) family of zinc metalloendopeptidases: genomics and function. *Bioessays* **23**, 261-269 (2001). https://doi.org:10.1002/1521-1878(200103)23:3<261::AID-BIES1036>3.0.CO;2-K

56 Esch, F. S. *et al.* Cleavage of amyloid beta peptide during constitutive processing of its precursor. *Science* **248**, 1122-1124 (1990). https://doi.org:10.1126/science.2111583

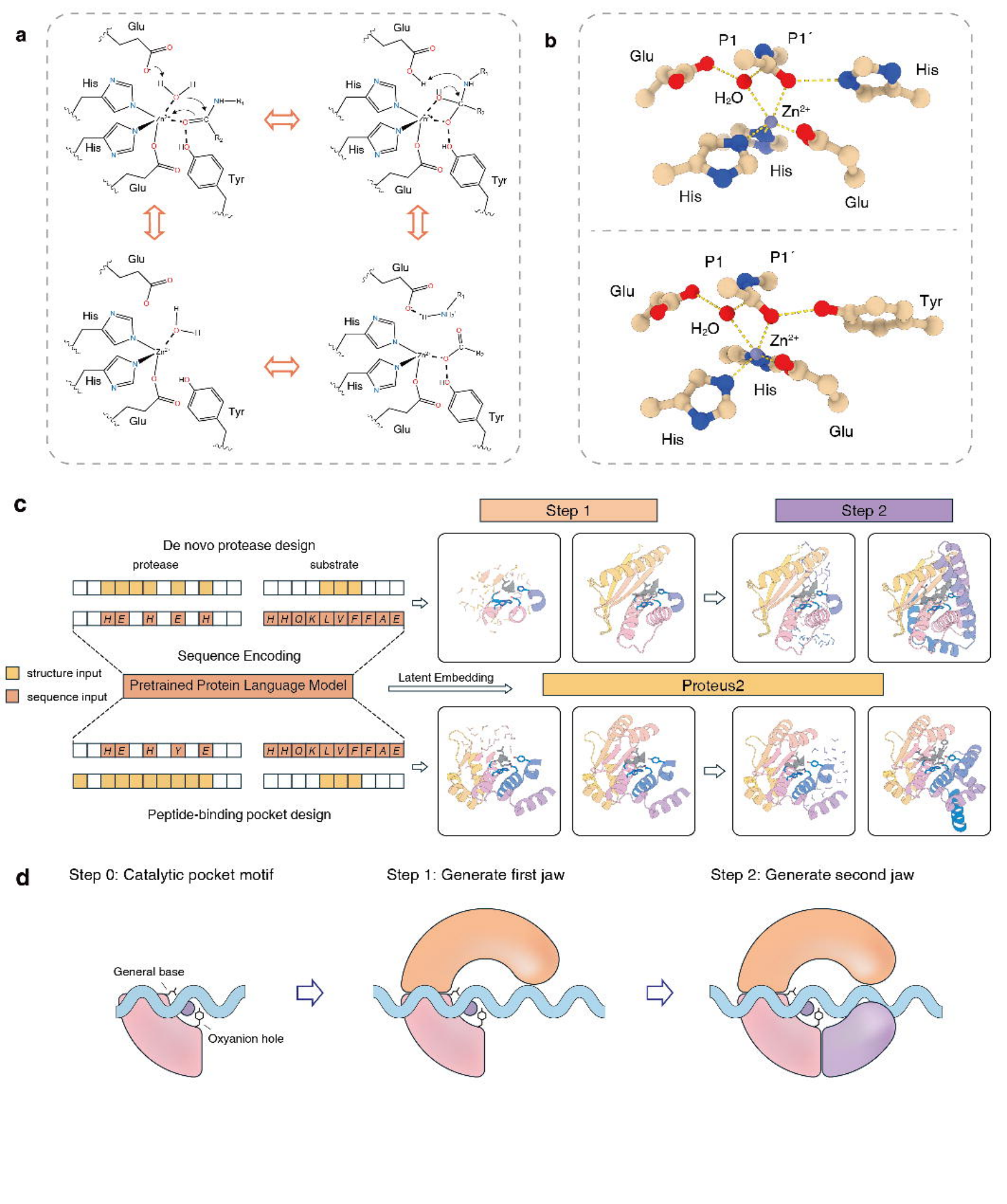
a
Glu
His
His
Glu
Tyr
b
P1
P1´
Glu
His
H2O
Zn2+
His
His
Glu
Tyr
c
Step 1
Step 2
De novo protease design
protease
substrate
H E H E H
H H Q K L V F F A E
Sequence Encoding
structure input
sequence input
Pretrained Protein Language Model
Latent Embedding
Proteus2
H E H Y E
H H Q K L V F F A E
Peptide-binding pocket design
d
Step 0: Catalytic pocket motif
Step 1: Generate first jaw
Step 2: Generate second jaw
General base
Oxyanion hole

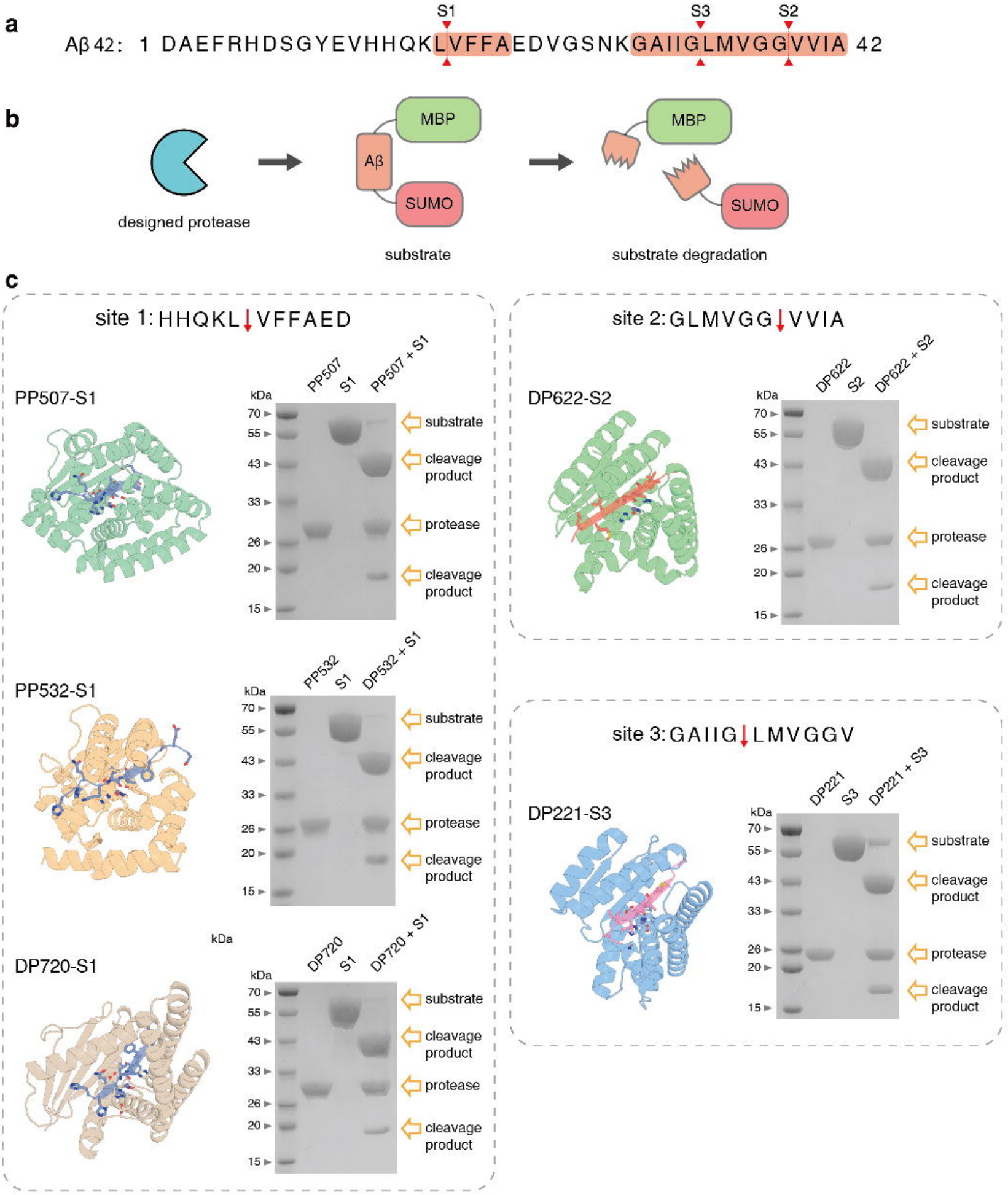
a
S1
S3
S2
Aβ42: 1 DAEFRHDSGYEVHHQKLVFFAEDVGSNKGAIIGLMVGGVVIA 42
b
designed protease
MBP
Aβ
SUMO
substrate
MBP
SUMO
substrate degradation
c
site 1: HHQKL↓VFFAED
PP507-S1
PP507
S1
PP507 + S1
kDa
70
55
43
33
26
20
15
substrate
cleavage product
protease
cleavage product
PP532-S1
PP532
S1
DP532 + S1
DP720-S1
DP720
S1
DP720 + S1
site 2: GLMVGG↓VVIA
DP622-S2
DP622
S2
DP622 + S2
site 3: GAIIG↓LMVGGV
DP221-S3
DP221
S3
DP221 + S3

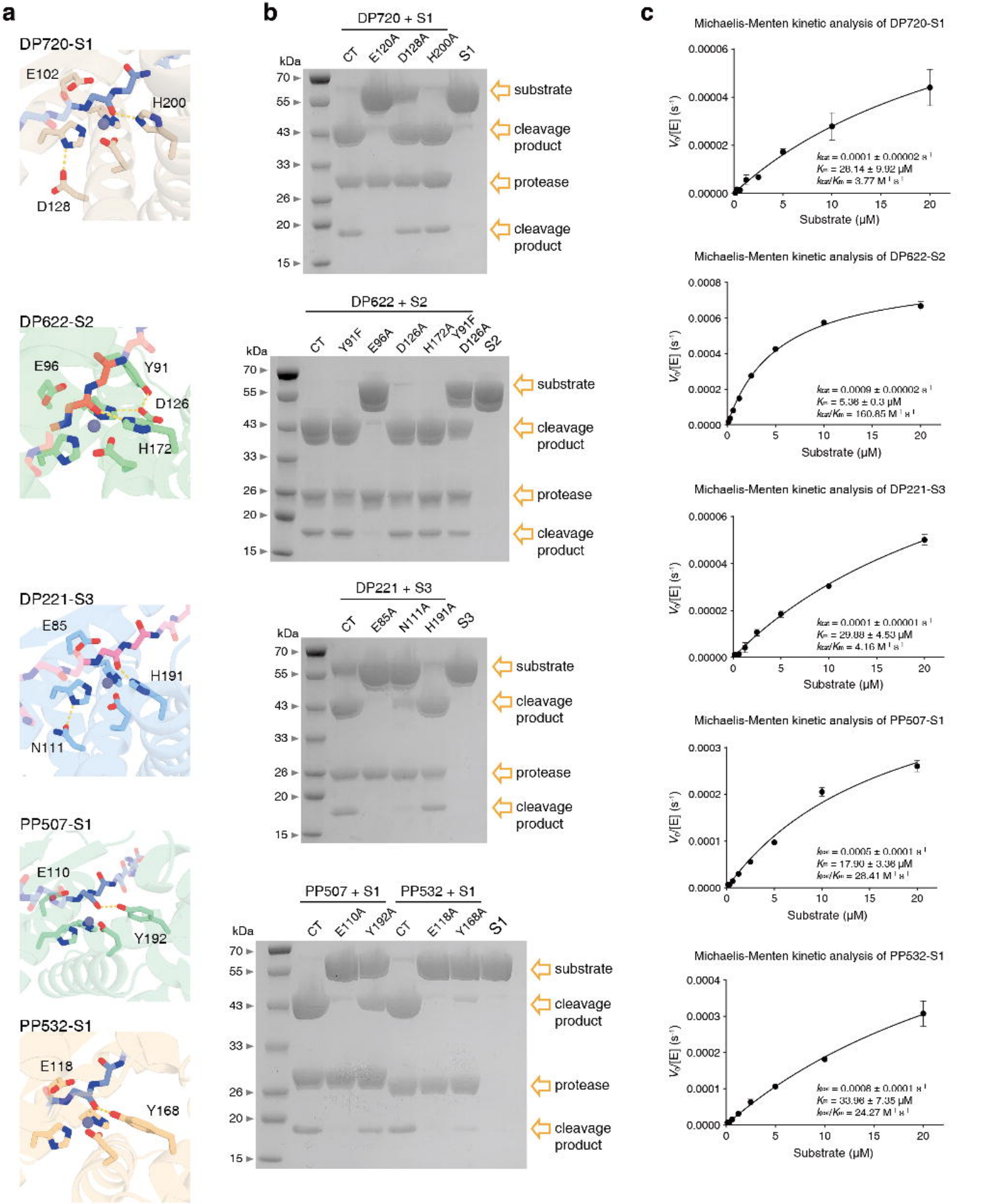
a
DP720-S1
E102
H200
D128
DP622-S2
E96
Y91
D126
H172
DP221-S3
E85
H191
N111
PP507-S1
E110
Y192
PP532-S1
E118
Y168
b
DP720 + S1
CT
E120A
D128A
H200A
S1
kDa
70
55
43
33
26
20
15
substrate
cleavage product
protease
cleavage product
DP622 + S2
CT
Y91F
E96A
D126A
H172A
Y91F D126A
S2
substrate
cleavage product
protease
cleavage product
DP221 + S3
CT
E85A
N111A
H191A
S3
substrate
cleavage product
protease
cleavage product
PP507 + S1
PP532 + S1
CT
E110A
Y192A
CT
E118A
Y168A
S1
substrate
cleavage product
protease
cleavage product
c
Michaelis-Menten kinetic analysis of DP720-S1
k_{cat} = 0.0001 ± 0.00002 s⁻¹
K_m = 28.14 ± 9.92 μM
k_{cat}/K_m = 3.77 M⁻¹ s⁻¹
Michaelis-Menten kinetic analysis of DP622-S2
k_{cat} = 0.0009 ± 0.00002 s⁻¹
K_m = 5.38 ± 0.3 μM
k_{cat}/K_m = 160.85 M⁻¹ s⁻¹
Michaelis-Menten kinetic analysis of DP221-S3
k_{cat} = 0.0001 ± 0.00001 s⁻¹
K_m = 29.88 ± 4.53 μM
k_{cat}/K_m = 4.16 M⁻¹ s⁻¹
Michaelis-Menten kinetic analysis of PP507-S1
k_{cat} = 0.0005 ± 0.0001 s⁻¹
K_m = 17.90 ± 3.36 μM
k_{cat}/K_m = 28.41 M⁻¹ s⁻¹
Michaelis-Menten kinetic analysis of PP532-S1
k_{cat} = 0.0008 ± 0.0001 s⁻¹
K_m = 33.96 ± 7.35 μM
k_{cat}/K_m = 24.27 M⁻¹ s⁻¹
$V_0/[E]$ (s⁻¹)
Substrate (μM)

a Cleavage of different substrates by DP720-S1

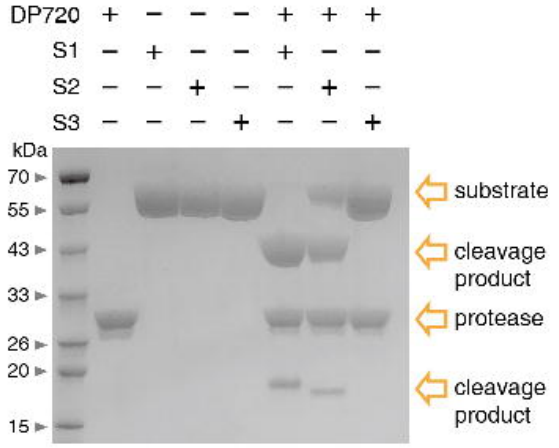

b Cleavage of different substrates by PP507-S1

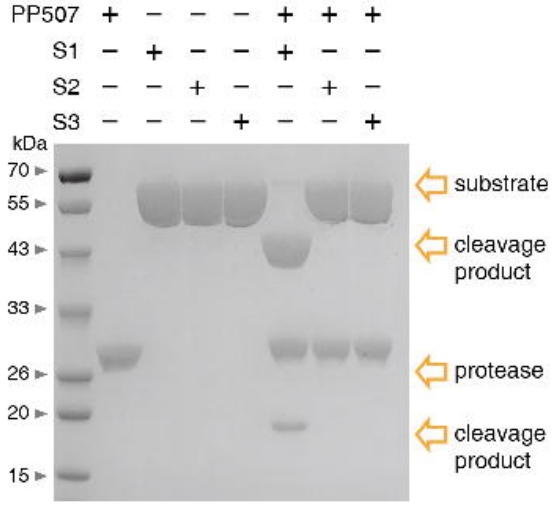

c Cleavage of different substrates by PP532-S1

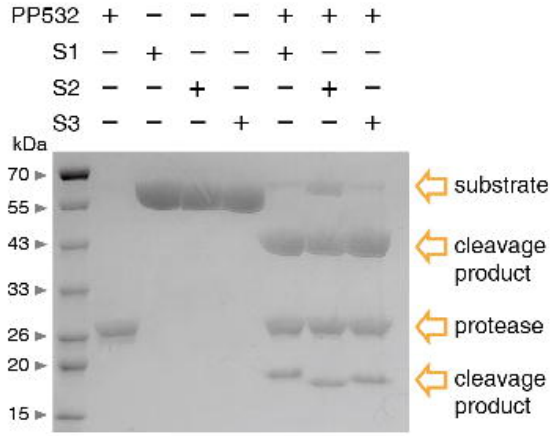

d Cleavage of different substrates by DP622-S2

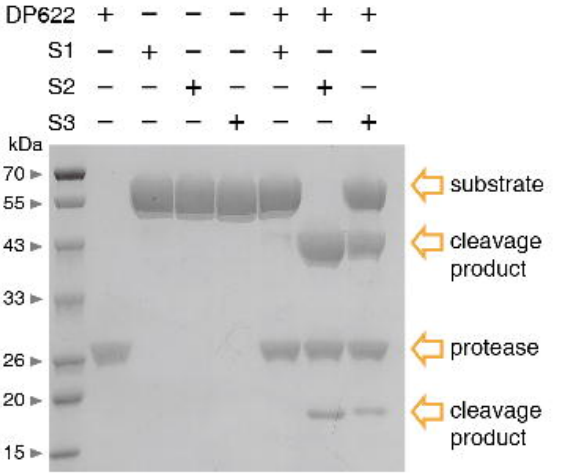

e Cleavage of different substrates by DP221-S3

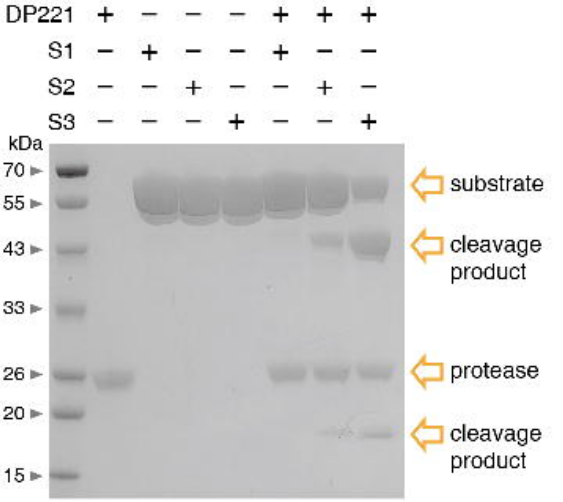

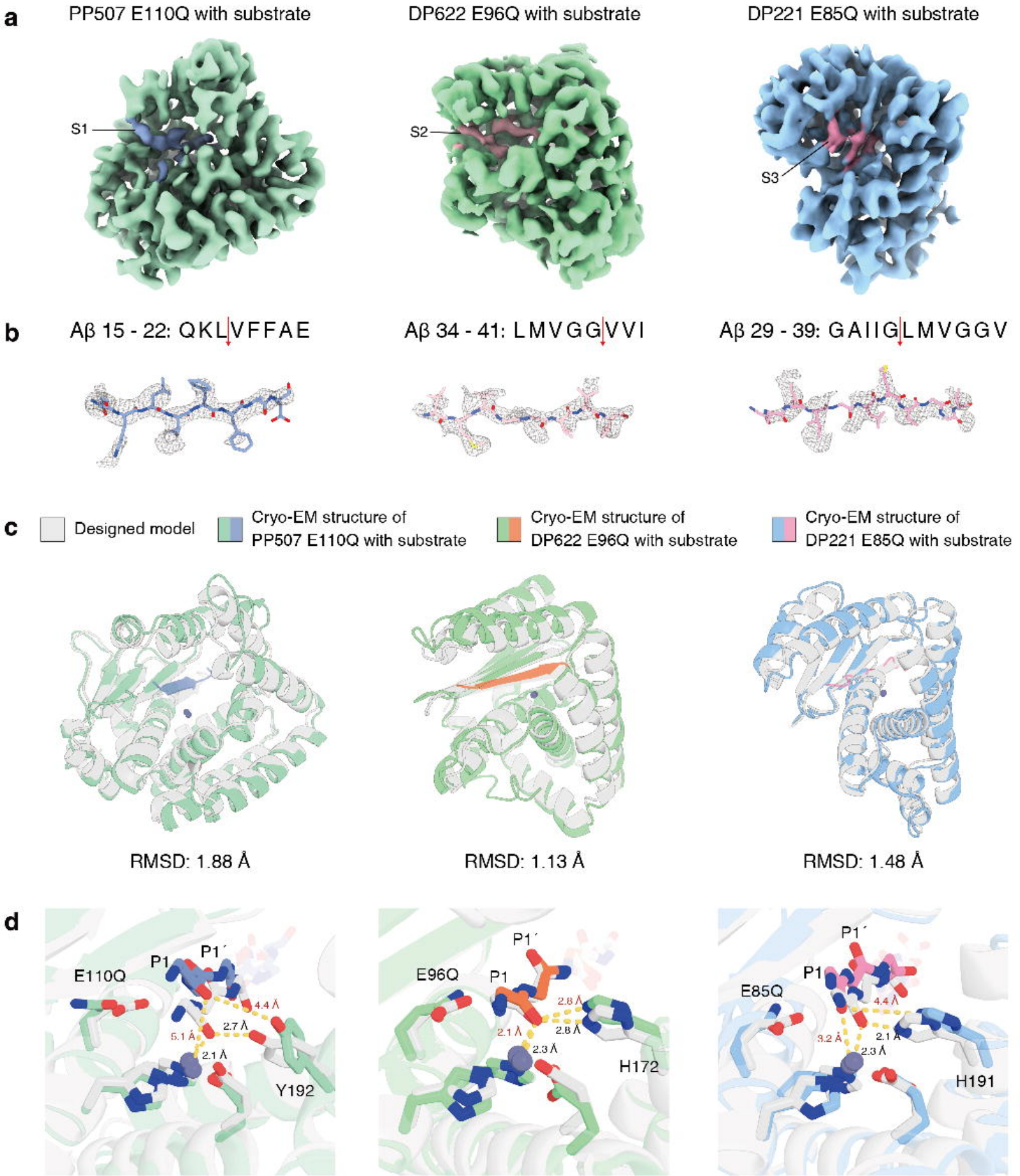
a
PP507 E110Q with substrate
DP622 E96Q with substrate
DP221 E85Q with substrate
S1
S2
S3
b
Aβ 15 - 22: QKL↓VFFAE
Aβ 34 - 41: LMVGG↓VVI
Aβ 29 - 39: GAIIG↓LMVGGV
c
Designed model
Cryo-EM structure of PP507 E110Q with substrate
Cryo-EM structure of DP622 E96Q with substrate
Cryo-EM structure of DP221 E85Q with substrate
RMSD: 1.88 Å
RMSD: 1.13 Å
RMSD: 1.48 Å
d
E110Q
P1
P1´
4.4 Å
2.7 Å
5.1 Å
2.1 Å
Y192
E96Q
P1
P1´
2.8 Å
2.8 Å
2.1 Å
2.3 Å
H172
E85Q
P1
P1´
4.4 Å
3.2 Å
2.1 Å
2.3 Å
H191